In vivo two-photon excited fluorescence microscopy reveals cardiac- and respiration-dependent pulsatile blood flow in cortical blood vessels in mice

Thom P. Santisakultarm, Nathan R. Cornelius, Nozomi Nishimura, Andrew I. Schafer, Richard T. Silver, Peter C. Doerschuk, William L. Olbricht and Chris B. Schaffer

Am J Physiol Heart Circ Physiol 302:H1367-H1377, 2012. First published 20 January 2012; doi:10.1152/ajpheart.00417.2011

Am J Physiol Heart Circ Physiol 302: H1367–H1377, 2012.
First published January 20, 2012; doi:10.1152/ajpheart.00417.2011.

In vivo two-photon excited fluorescence microscopy reveals cardiac- and respiration-dependent pulsatile blood flow in cortical blood vessels in mice

Thom P. Santisakultarm (ธม สันติสกุลธรรม),[1] Nathan R. Cornelius,[1] Nozomi Nishimura,[1] Andrew I. Schafer,[2] Richard T. Silver,[2] Peter C. Doerschuk,[1,3] William L. Olbricht,[1,4] and Chris B. Schaffer[1]

[1]*Department of Biomedical Engineering, Cornell University, Ithaca;* [2]*Department of Medicine, Weill Cornell Medical College, New York; and Departments of* [3]*Electrical and Computer Engineering and* [4]*Chemical and Biomolecular Engineering, Cornell University, Ithaca, New York*

Submitted 25 April 2011; accepted in final form 13 January 2012

Santisakultarm TP, Cornelius NR, Nishimura N, Schafer AI, Silver RT, Doerschuk PC, Olbricht WL, Schaffer CB. In vivo two-photon excited fluorescence microscopy reveals cardiac- and respiration-dependent pulsatile blood flow in cortical blood vessels in mice. *Am J Physiol Heart Circ Physiol* 302: H1367–H1377, 2012. First published January 20, 2012; doi:10.1152/ajpheart.00417.2011.—Subtle alterations in cerebral blood flow can impact the health and function of brain cells and are linked to cognitive decline and dementia. To understand hemodynamics in the three-dimensional vascular network of the cerebral cortex, we applied two-photon excited fluorescence microscopy to measure the motion of red blood cells (RBCs) in individual microvessels throughout the vascular hierarchy in anesthetized mice. To resolve heartbeat- and respiration-dependent flow dynamics, we simultaneously recorded the electrocardiogram and respiratory waveform. We found that centerline RBC speed decreased with decreasing vessel diameter in arterioles, slowed further through the capillary bed, and then increased with increasing vessel diameter in venules. RBC flow was pulsatile in nearly all cortical vessels, including capillaries and venules. Heartbeat-induced speed modulation decreased through the vascular network, while the delay between heartbeat and the time of maximum speed increased. Capillary tube hematocrit was 0.21 and did not vary with centerline RBC speed or topological position. Spatial RBC flow profiles in surface vessels were blunted compared with a parabola and could be measured at vascular junctions. Finally, we observed a transient decrease in RBC speed in surface vessels before inspiration. In conclusion, we developed an approach to study detailed characteristics of RBC flow in the three-dimensional cortical vasculature, including quantification of fluctuations in centerline RBC speed due to cardiac and respiratory rhythms and flow profile measurements. These methods and the quantitative data on basal cerebral hemodynamics open the door to studies of the normal and diseased-state cerebral microcirculation.

microcirculation; hemodynamics; intravital imaging; vessel bifurcation; brain

THE COMPLEX, THREE-DIMENSIONAL (3-D) vascular architecture of the brain presents a challenge to studies of microvascular hemodynamics. Larger arterioles form a net at the cortical surface and give rise to penetrating arterioles that plunge into the brain and feed capillary networks, where most nutrient and metabolite exchange occurs (2). These capillaries coalesce into ascending venules, which return to the cortical surface and drain into larger surface venules (22). Several lines of evidence have suggested that even small changes in hemodynamics in the brain can have detrimental impacts on the health and function of neurons. Chronic diseases that alter the microcirculation, such as hypertension (24) and diabetes (7), are risk factors for dementia and have been linked to cognitive decline (33). Flow disruptions from hyperviscous blood in diseases such as polycythemia vera and essential thrombocythemia are linked to neural degeneration (16). In addition, occlusion of cerebral microvessels may cause the small, clinically silent, strokes that have been associated with cognitive impairment and are a risk factor for dementia (34). Furthermore, decreases in the pulsatility of blood flow result in higher systemic vascular resistance, decreased O_2 metabolism, and reduced efficiency of the microcirculation (51). Novel methods that enable the quantification of blood flow and vascular changes at the level of individual microvessels in the complex cortical vasculature would greatly improve our understanding of the causes and consequences of such microvascular pathologies as well as provide insights into normal-state hemodynamic regulation.

The most extensive data on blood flow dynamics in microvascular networks come from two-dimensional (2-D) vascular beds, such as the cremaster muscle, omentum, and mesentery, where experimental techniques such as wide-field intravital microscopy can be readily applied. In these systems, studies of average blood flow speed in individual microvessels (54), the distribution of red blood cells (RBCs) at microvascular junctions (36), and flow pulsatility in capillaries (54) have been made. These data have fueled detailed modeling of blood flow dynamics in microcirculatory networks that has elucidated the biophysical and physiological principles that govern flow (1, 11, 35, 42).

In early studies of brain microcirculation, the average flow speed and pulsatility of flow in cortical surface vessels was characterized (38), and more recent work has measured flow profiles in pial arterioles using Doppler optical coherence tomography (46). However, because of the 3-D vascular architecture of the brain, techniques with the ability to resolve flow in microvessels at different depths in the tissue are required to quantify flow dynamics throughout the vascular hierarchy. Recently, two-photon excited fluorescence (2PEF) microscopy has emerged as an approach to quantify flow changes in individual cortical microvessels in response to neural activity (20) and microvascular occlusion (30, 31, 40), with the potential to access vessels throughout the full cortical thickness of a mouse (21). However, the careful quantification of blood flow dynamics that has been done in 2-D microvascular beds has not yet been performed in the brain vascular network. For example,

Address for reprint requests and other correspondence: C. B. Schaffer, Dept. of Biomedical Engineering, Cornell Univ., B57 Weill Hall, Ithaca, NY 14853 (e-mail: cs385@cornell.edu).

previous work has not mapped average flow speed or heartbeat-induced flow modulation in vessels throughout the cortical network, measured spatial flow profiles in brain microvessels, or quantified important hemodynamic parameters, such as pulse wave velocity.

Our work aimed to overcome the challenges of quantifying blood flow dynamics in 3-D microvascular networks in live animal models. We coupled electrocardiogram (ECG) and respiratory waveform measurements with 2PEF-based assessment of RBC speed in individual vessels in anesthetized mice. We quantified average centerline RBC flow speed as well as temporal flow fluctuations due to cardiac and respiratory rhythms in cortical arterioles, capillaries, and venules. Interestingly, we found pulsatile RBC flow in vessels throughout the cortical network, including capillaries and venules, and identified respiration-dependent changes in cortical blood flow. We quantified the tube hematocrit in brain capillaries and found no dependence on centerline RBC speed or position in the vascular hierarchy. We also measured time- and space-dependent RBC flow profiles in arterioles, in venules, and at vascular junctions and found that spatial flow profiles were blunted in most vessels. These data provide a detailed quantification of cerebral hemodynamics in brain microvessels, while the methods we developed open the door to future studies of alterations in brain hemodynamics due to cerebrovascular disease.

MATERIALS AND METHODS

Animals and surgical preparation. We used 19 male and 3 female adult (3–7 mo old) wild-type C57BL/6 mice (weight: 18–31 g) in this study. Animals were anesthetized with 5% isoflurane in O_2 and maintained at 1.5–2% during surgery and imaging. Glycopyrrolate (0.05 mg/100-g mouse) was intramuscularly injected to facilitate respiration. Bupivacaine (0.1 ml, 0.125%) was subcutaneously administered at the incision site to provide local anesthesia. A 5-mm craniotomy was prepared over the parietal cortex. An 5-mm diameter, no. 1.5 glass coverslip (50201, World Precision Instruments) was glued to the skull using cyanoacrylate (Loctite) and dental cement (Co-Oral-Ite Dental). The space between the exposed brain and the coverglass was filled with artificial cerebrospinal fluid (19). Mouse body temperature was maintained at 37.5°C with a feedback-controlled heating blanket (50-7053P, Harvard Apparatus). Animals received 5% (wt/vol) glucose in physiological saline (0.5 ml/100-g mouse) hourly. To fluorescently label the vasculature, 0.1 ml of a 2.5% (wt/vol) solution of 70-kDa Texas red-dextran (D1830, Invitrogen) or 70-kDa fluorescein-conjugated dextran (FD70S, Sigma) in physiological saline was injected retroorbitally. The resulting dextran concentration in the blood was ~0.0015 g/ml, well below the concentration required to trigger RBC aggregation (27). No RBC aggregation was observed in our experiments. The care and experimental manipulation of our animals were reviewed and approved by the Institutional Animal Care and Use Committee of Cornell University.

In vivo 2PEF imaging of cerebral blood vessels. Images were obtained using a custom-built 2PEF microscope that used a train of 1,040-nm, 1-MHz, 300-fs pulses from a Yb-fiber chirped pulse amplifier (FCPA μJewel D-400, IMRA America) for two-photon excitation of Texas red or a train of 800-nm, 87-MHz, 100-fs pulses from a Ti:sapphire laser oscillator (MIRA HP, pumped by a Verdi-V18, Coherent) for fluorescein. The laser pulses were scanned in a raster pattern by galvanometric mirrors imaged to the back aperture of the objective. 2PEF was reflected by a dichroic mirror and relayed to a photomultiplier tube through a filter centered at 645 or 517 nm, both with 65-nm bandwidth, for Texas red and fluorescein imaging, respectively. Laser scanning and data acquisition were controlled by MPScope software (29). Low-magnification images of the vasculature in the entire cranial window were taken using a ×4 (numerical aperture: 0.28) air objective (Olympus; Fig. 1*A*). For high-resolution imaging (Fig. 1*B*), vessel diameter measurements (Fig. 1, *C* and *D*), and RBC flow speed measurements (Fig. 1, *E* and *F*), we used a ×20 (numerical aperture: 0.95) water-immersion objective (Olympus).

To map vascular topology and determine vessel classes (i.e., arteriole vs. capillary vs. venule), stacks of images spaced 1 μm axially through the top 350 μm of the cortex were obtained (Fig. 1*B*). Penetrating arterioles were identified as vessels that branched from readily identifiable surface arterioles and plunged vertically into the brain. We confirmed that the flow was into the brain using line-scan measurements (see below). Similarly, ascending venules had flow that emerged from the brain and drained into readily identifiable surface venules. We classed all subsurface vessels

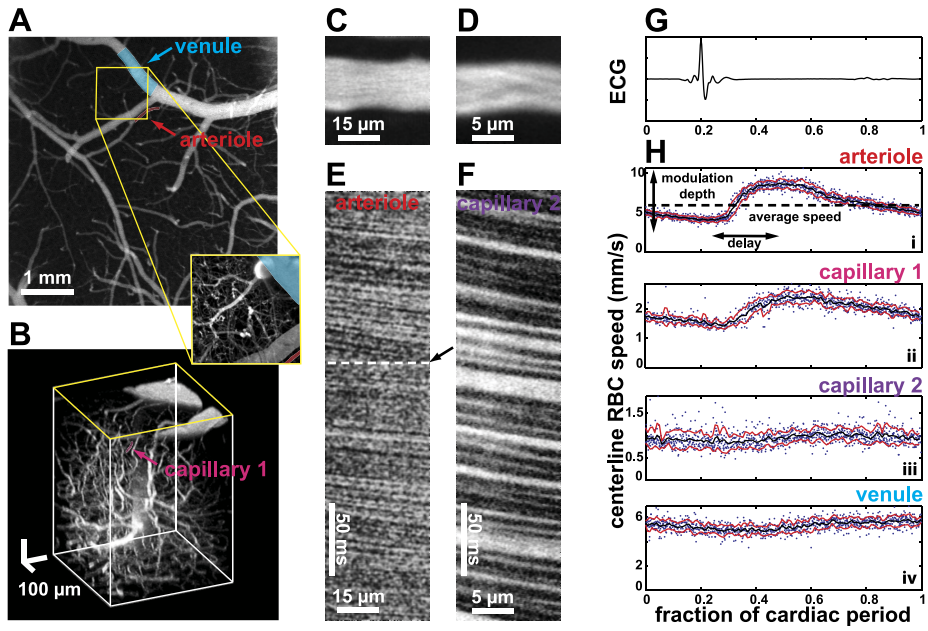

Fig. 1. In vivo two-photon excited fluorescence (2PEF) imaging of vascular topology and cerebral blood flow during the cardiac cycle. *A*: low-magnification 2PEF image of the fluorescently labeled brain vasculature in an anesthetized mouse. *B*: three-dimensional rendering of the vasculature with the brain surface at the top of the image. *C–F*: Axially projected image of an arteriole (*C*) and a capillary (*D*) with their line-scan images (*E* and *F*, respectively). The arrow in *E* indicates the red blood cell (RBC) flow speed increase due to a heartbeat. *G*: ECG used to align the flow speed data. *H*: centerline RBC speed of an arteriole (*i*), two capillaries (*ii* and *iii*), and a venule (*iv*) as a function of time, expressed as a fraction of the cardiac cycle. The colors of the vessel labels in *H* correspond to the colored highlights in the 2PEF and line-scan images.

branching from penetrating arterioles and ascending venules as capillaries and determined the number of capillary segments separating each capillary from the topologically nearest penetrating arteriole or ascending venule. The depth of each capillary was measured relative to the middle of the cortical surface vessels. We measured blood flow speed and the diameter of surface vessels and capillaries up to 10 branches downstream and upstream from penetrating and ascending vessels, respectively. To determine vessel diameter, we recorded images of individual vessels stepping from above to below the vessel. These images were averaged, and diameters were calculated by manually selecting a portion of the vessel, calculating the area above threshold (20% of maximum intensity), and divided this by the length of the selected segment.

2PEF measurement of RBC flow speed. The intravenously injected dye labels only the blood plasma, so RBCs appear as moving dark patches within the vessel lumen. Tracking the motion of these dark patches enables the measurement of centerline RBC flow speed. We tracked RBC motion by repetitively scanning a line along the central axis of single vessels at a line rate of 1.7 kHz for at least 30 s (20, 40). The space-time image produced by the line scan contained diagonal dark streaks formed by moving RBCs, with a slope that was inversely proportional to the centerline RBC speed (Fig. 1, *E* and *F*).

Determination of RBC flow speed from line-scan images. To quantify RBC speed in individual vessels from the space-time images, we used a Radon transform-based algorithm similar to that of Drew et al. (10). Low spatial frequency components in the line-scan image were filtered with a high-pass isotropic Gaussian filter. The frequency response of the filter was 1 minus a scaled Gaussian, centered at zero frequency, with a diagonal covariance matrix with values of 25 pixel^{-2}, and the scaling was set so that the frequency response at zero frequency was zero. Eliminating low-frequency components, such as vertical streaks in the space-time image that arise from stationary artifacts in the blood vessel, greatly decreased the amount of noise and accentuated the difference between the dark and light streaks formed by moving RBCs.

$$g(\rho, \theta) = \int_{-\infty}^{\infty}\int_{-\infty}^{\infty} g(x, y)\delta(\rho - x\cos\theta - y\sin\theta)\,dx\,dy \qquad (1)$$

We then performed a Radon transform on the filtered data, which computes line integrals of a 2-D function [$g(x,y)$] at different angles (θ) from 0° to π with respect to the y-axis and at different radial offsets from the origin (ρ) to yield a new function [$g(\rho, \theta)$]. δ is the Dirac delta function. When $\theta = \theta^*$ matches the angle of the streaks in a line-scan image, the fluctuations of $g(\rho,\theta^*)$ with respect to ρ are greatest. To identify θ^*, we found the value of θ where the variance along the ρ-axis was a maximum. The RBC speed was then equal to $\tan^{-1}\theta^*$ multiplied by time and length coefficients, which depend on the line-scan rate and the spatial extent of the line-scan image. For vessels on the brain surface, the image plane was aligned with the plane of the vessel. For subsurface capillaries, there was sometimes a small angle between the image plane and the vessel. These angles were measured from the 3-D image stacks for each capillary, and the calculated centerline RBC flow speed was divided by the cosine of this angle.

Alignment of flow speed measurements to the cardiac cycle. To measure the temporal centerline RBC flow profile during a cardiac cycle, we placed intramuscular leads in the animal's left anterior and right posterior limbs. The ECG signal was amplified (ISO-80 Bio-Amplifier, World Precision Instruments) and recorded (3.4-kHz sampling rate) simultaneously with the line-scan data (Fig. 1*G*). The temporal locations of R waves (identified by thresholding) in the ECG signal were used as markers to align centerline RBC speed measurements from each cardiac cycle. A moving average of the RBC flow speed over the cardiac cycle was computed with a window size of ~1.5% of the cardiac cycle (Fig. 1*H*). The modulation depth of the flow speed was calculated by normalizing the difference between the maximum and minimum flow speeds across the cardiac cycle by the average flow speed. A vessel was designated as having no flow modulation if the difference between maximum and minimum centerline RBC flow speeds was less than the SD of the speed across the cardiac cycle. The delay between heartbeat (R wave) and the time of maximal flow speed for vessels with flow modulation was calculated and normalized by the average time between heartbeats. This delay was aggregated across multiple vessels and animals by temporally aligning all measurements using the R wave of the ECG.

Estimation of capillary tube hematocrit. Tube hematocrit (Hct_{tube}) was calculated as follows (6):

$$Hct_{tube} = \frac{fV_{RBC}}{v\pi R^2} \qquad (2)$$

where f is RBC flux, V_{RBC} is the mean corpuscular volume of mouse RBCs, v is centerline RBC speed, and R is the vessel radius. RBC flux was extracted from line-scan data by manually counting the number of cells in ten 0.3-s time segments, which were spaced by 3 s throughout the measurement. We only included vessels with single-file RBC motion, where each RBC made a distinct streak in the space-time image. This excluded all capillaries with RBC flux above 270 RBCs/s, where the manual counting of RBC flux was unreliable. We took the mean corpuscular volume of mouse RBCs to be 45 μm^3 (15).

Spatial blood flow profile measurement. To obtain a spatial RBC flow profile in individual surface vessels, line scans were sequentially recorded as a function of lateral position, from one vessel wall to the other with a step size of 2–4 μm, all in a horizontal plane located at the depth where the vessel was widest. The blood flow speed data from all line-scan measurements was temporally aligned using the ECG to obtain time- and space-dependent flow profiles in individual vessels (see Fig. 5). The data were smoothed first temporally and then spatially using moving averages with a temporal width of ~1.5% of the cardiac cycle and a spatial extent of three adjacent line scans, respectively. For each vessel, the spatial flow speed profile [$v(r)$] was fit using the following equation (47):

$$v(r) = v_{max}\left(1 - \left|\frac{r}{R}\right|^k\right) \qquad (3)$$

where v_{max} is the maximum flow speed, r is the distance from the center of the vessel, k is the degree of blunting (a value of 2 corresponds to a parabolic profile), and R is the vessel radius. Similar measurements were made before, at, and after bifurcations or mergers in surface arterioles and venules, respectively (see Fig. 6). In arteriole (venule) measurements, the RBC speed profile in the upstream vessel(s) was characterized about one vessel diameter upstream from the bifurcation (merger), whereas downstream branch(es) were characterized immediately after the bifurcation (merger).

Alignment of flow speed measurements to the respiratory cycle. To measure the temporal RBC flow speed profile during each respiratory cycle, a breathing signal was recorded simultaneously with ECG and line-scan data using a locally designed breathing sensor. Briefly, an 805-nm light-emitting diode (LED) illuminated the back of the mouse above the chest cavity from a distance of ~1 cm. The amplitude of the LED emission was sinusoidally modulated at 2 kHz. A photodiode located adjacent to the LED detected the light reflected from the animal. The photodiode signal was amplified using a lock-in amplifier (SR530, Stanford Research Systems) with a 30-ms time constant using the 2-kHz LED modulation as a reference. As the animal inhaled and exhaled, the amount of light reaching the photodiode changed slightly, allowing continuous monitoring of the breathing waveform (see Fig. 7*A*, *top*). Line-scan data were recorded concurrently with both ECG and breath signals for 10 min. To align RBC flow speed data with the respiratory cycle, we used the same method described for cardiac cycle alignment but using the inspiration signal as the alignment marker (see Fig. 7*B*). To align the flow speed data with both the cardiac and respiratory waveforms, we used R waves of the ECG

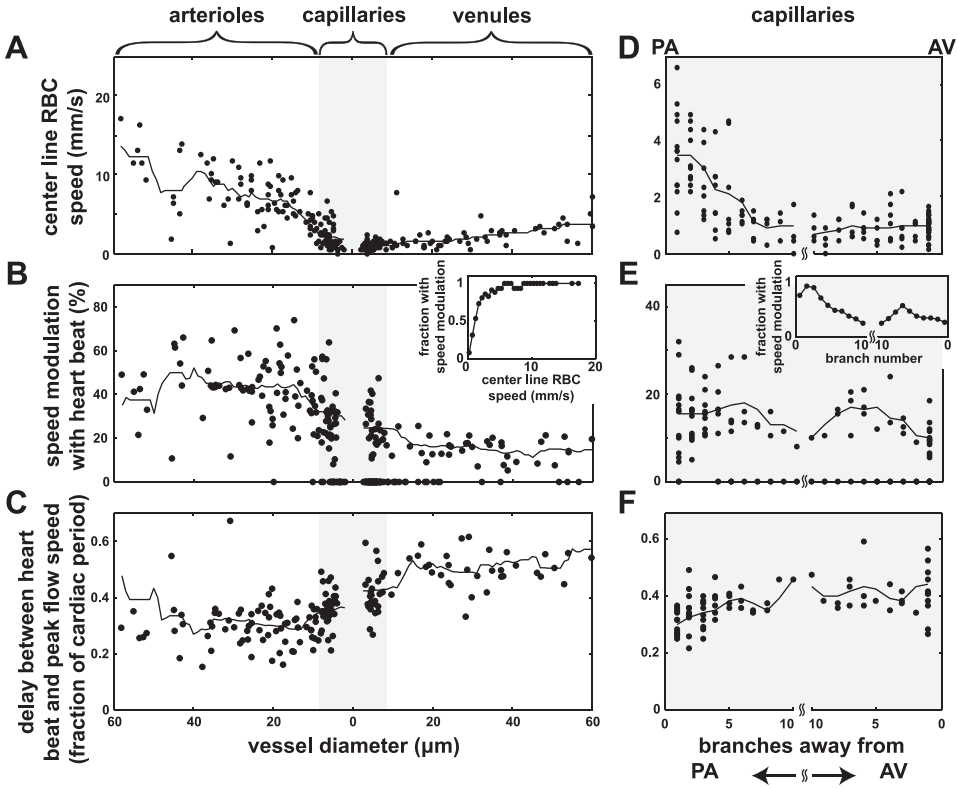

Fig. 2. Average centerline RBC speed, flow speed modulation, and delay to maximal flow speed for cerebral microvessels. *A–C*: average centerline RBC speed (*A*), flow speed modulation with heartbeat (*B*), and delay between heartbeat and time of maximal flow speed (*C*) as a function of vessel diameter. To display the progression of blood flow through the vascular network, data for arterioles (venules) are displayed on the *left* (*right*) portion of the plot with decreasing (increasing) diameter. Capillaries are toward the *middle* and are placed to the arteriole or venule side based on which they are topologically closer to. *D–F*: average centerline RBC speed (*D*), flow speed modulation with heartbeat (*E*), and delay between heartbeat and time of maximal flow speed (*F*) for capillaries as a function of topological connectivity to penetrating arterioles (PA) from the *left* side and to ascending venules (AV) from the *right* side.

signal and inspiration peaks of the respiratory signal as markers and binned each flow speed measurement into a 2-D matrix that specified the measurement time with respect to both heartbeat and inspiration. The data were then smoothed using a rectangular 2-D moving average that had a width of 5% of the cardiac cycle and a length of 5% of the respiratory cycle. The data were used to create a 3-D plot that decoupled the RBC flow speed dependence on heartbeat and breathing (see Fig. 7, *D* and *E*).

RESULTS

Temporal blood flow fluctuations due to rhythmic cardiac contractions. We used 2PEF imaging of the fluorescently labeled vasculature in craniotomized, anesthetized mice to quantify the temporal blood flow dynamics in cortical microvessels. Vascular topology was traced in 3-D image stacks to identify surface and penetrating arterioles, capillaries, and ascending and surface venules (Fig. 1, *A* and *B*). We measured diameter and centerline RBC flow speed (by tracking RBC motion) in individual arterioles (Fig. 1, *C* and *E*), capillaries (Fig. 1, *D* and *F*), and venules. RBC speed measurements in each vessel were temporally aligned to heartbeat (Fig. 1*H*). The average cardiac period was 0.14 ± 0.04 s (mean ± SD), which corresponds to a heart rate of 430 ± 100 beats/min (20 mice). Arteriole temporal centerline RBC flow profiles typically displayed a clear speed modulation with heartbeat (Fig. 1*H*,*i*), whereas capillaries (Fig. 1*H*,*ii*) and venules (Fig. 1*H*,*iv*) showed smaller modulation depth, with speed modulation not detectable above noise in some capillaries (Fig. 1*H*,*iii*) and venules. The delay between the heartbeat and the time of maximum centerline RBC flow speed was shortest in arterioles, followed by capillaries and then venules (Fig. 1*H*).

Quantification of average RBC flow speed and heartbeat-dependent speed fluctuations. We measured temporal RBC speed profiles in microvessels throughout the cortical vascular hierarchy. Centerline RBC flow speed (averaged over ~200 cardiac cycles) significantly decreased (from 13 to 3 mm/s) with decreasing diameter (from 60 to 10 μm) in surface and penetrating arterioles [66 vessels, 14 animals, $P < 0.0003$ by Cuzick's trend test (8); Fig. 2*A*]. Capillaries (<10-μm diameter) exhibited the slowest RBC flow speeds of 1.5 ± 1.2 mm/s (156 vessels, 17 animals), with capillaries topologically closer to arterioles, having significantly higher flow speeds than those closer to venules ($P < 0.0001$ by Cuzick's trend test; Fig. 2*D*). We found no dependence of capillary blood flow speed on the depth of the vessel beneath the cortical surface (Fig. 3). Flow speed significantly increased (from 1 to 4 mm/s) with increasing vessel diameter (from 10 to 60 μm) in ascending and

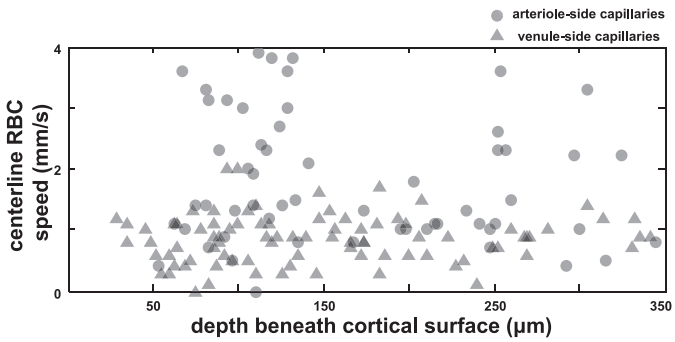

Fig. 3. Capillary RBC flow speed as a function of depth beneath the cortical surface.

surface venules (56 vessels, 14 animals, $P < 0.0001$ by Cuzick's trend test) but remained slow compared with arterioles ($P < 0.0001$ by two-sided *t*-test; Fig. 2*A*). The average magnitude of the centerline RBC flow speed modulation with heartbeat decreased continuously from arterioles (43 ± 15%, 61 vessels) to capillaries (28 ± 12%, 81 vessels) to venules (10 ± 8%, 54 vessels, $P < 0.0001$ by ANOVA; Fig. 2, *B* and *E*). Flow modulation was undetectable in many of the slower vessels (Fig. 2*B*, *inset*), especially in capillaries topologically further from penetrating arterioles (Fig. 2*E*, *inset*). Nearly all venules exhibited some modulation in blood flow speed with heartbeat. The delay between heartbeat and the time of maximum RBC flow speed significantly increased for vessels topologically further away from the heart ($P < 0.0001$ by Cuzick's trend test; Fig. 2, *C* and *F*).

Capillary tube hematocrit. We manually counted RBC flux in the line-scan data and determined the tube hematocrit of many of the capillaries using *Eq. 2*. We found that the average capillary hematocrit was 0.22 ± 0.19 ($n = 97$ capillaries), with a weak tendency for hematocrit to increase for smaller diameter vessels ($P = 0.0005$ by Cuzick's trend test; Fig. 4*A*), where RBCs deform significantly as they squeeze through the capillary and thus occupy a larger volume fraction. Tube hematocrit did not depend on the mean centerline flow speed in the capillary over the narrow range of flow speeds investigated (6) (Fig. 4*B*) or on the topological position of the capillary in the vascular bed (Fig. 4*C*).

Spatial blood flow profiles during a cardiac cycle. Spatial RBC flow profiles were obtained in vessels by measuring RBC flow speed at different positions within the vessel lumen. In both arterioles (Fig. 5*B*) and venules (Fig. 5*C*), flow speed was fastest in the center of the vessel and decreased toward the vessel walls. In both vessel classes, the spatial RBC flow profile was slightly blunted (average blunting index: 3.3 ± 1.1 in arterioles and 3.7 ± 1.5 in venules) compared with the parabolic flow profile expected for steady laminar flow (Fig. 5, *B*,*iii* and *C*,*iii*). In arterioles, the degree of blunting was significantly higher at diastole (average blunting index: 3.4 ± 1.1) compared with systole (average blunting index: 3.1 ± 1.1, $P = 0.002$ by paired *t*-test). Vessels with slower flow speeds tended toward increased blunting regardless of vessel class or cardiac phase (Fig. 5*D*).

We measured spatial RBC flow speed profiles upstream from, at, and downstream from surface arteriole bifurcations (Fig. 6*A*) and surface venule mergers (Fig. 6*C*). At the arteriole bifurcation, a spatial flow profile with two peaks was observed, whereas the peaks in the downstream branches were shifted laterally toward the outer sides of the vessels (Fig. 6*B*). Similarly, at the venule merger, a double-peaked flow profile was observed (Fig. 6*D*). We found that RBC flux (calculated assuming an axially symmetric flow profile) was conserved to within 30% and 11% in the arteriole and venule junctions, respectively. These errors likely reflect the fact that there was some physiological drift during the ~1-h time required to take all the necessary line-scan measurements and that the downstream flow profiles this close to a junction are likely not fully axially symmetric. Because our approach for measuring flow speed relies on tracking RBC motion, the flow profiles shown in Figs. 5 and 6 are effectively spatially averaged over the ~7-μm size of an RBC. This averaging likely reduces the depth of the dip in flow speed observed at the center of the flow profile in the bifurcation and merger shown in Fig. 6, *B* and *D*, respectively.

Temporal blood flow fluctuations due to breathing. In two animals, we measured centerline RBC flow speed in surface arterioles and venules while monitoring both respiration and heartbeat (Fig. 7*A*) and then aligned the flow speed data with respect to both respiratory (Fig. 7*B*) and cardiac (Fig. 7*C*) cycles. In arterioles (Fig. 7*D*) and venules (Fig. 7*E*), we observed a 33 ± 5% (3 vessels, 2 animals) and 29 ± 15% (3 vessels, 2 animals) decrease in blood flow speed just before inhalation (defined by chest wall motion), respectively (Fig. 7*F*). This flow speed decrease was preserved at all phases of the cardiac cycle and occurred significantly earlier in arterioles (0.08 ± 0.004 of a breath period before inhalation) than in venules (0.05 ± 0.012, $P = 0.004$ by two-tailed *t*-test; Fig. 7*G*). To rule out motion artifacts as a source of this observation, we measured RBC flow speed at locations shifted by ~10 μm horizontally and vertically from the center axis of an arteriole and found a similar decrease in flow speed just before inspiration at all locations (Fig. 8).

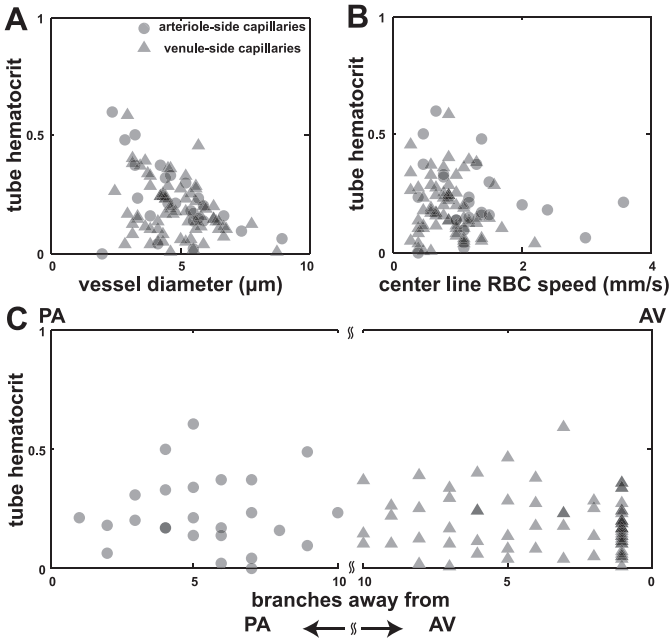

Fig. 4. Capillary tube hematocrit in the cortical microvascular network. *A–C*: tube hematocrit as a function of capillary diameter (*A*), centerline RBC speed (*B*), and topological connectivity (*C*) to PAs from the *left* side and to AVs from the *right* side.

DISCUSSION

Average RBC flow speed in cerebral vessels. We quantified centerline RBC flow speed in vessels throughout the cortical vascular hierarchy, starting from surface and penetrating arterioles, continuing to capillaries within the 3-D network deep in the cortex, and finally to ascending and surface venules. As expected, centerline RBC flow speed decreased with decreasing vessel diameter in arterioles, further slowed in capillaries, and then increased slightly with increasing vessel diameter in venules (Fig. 2*A*). In capillaries, flow speeds decreased about threefold over the first five capillary branches downstream from penetrating arterioles and then remained relatively uniform, at ~1 mm/s, through the rest of the capillary bed (Fig.

2*D*), with no dependence on depth beneath the cortical surface (Fig. 3). The average flow speeds for different class vessels measured here agree well with previous measurements of cerebral blood flow in rodents for arterioles (31, 40), capillaries (20), and venules (28, 38).

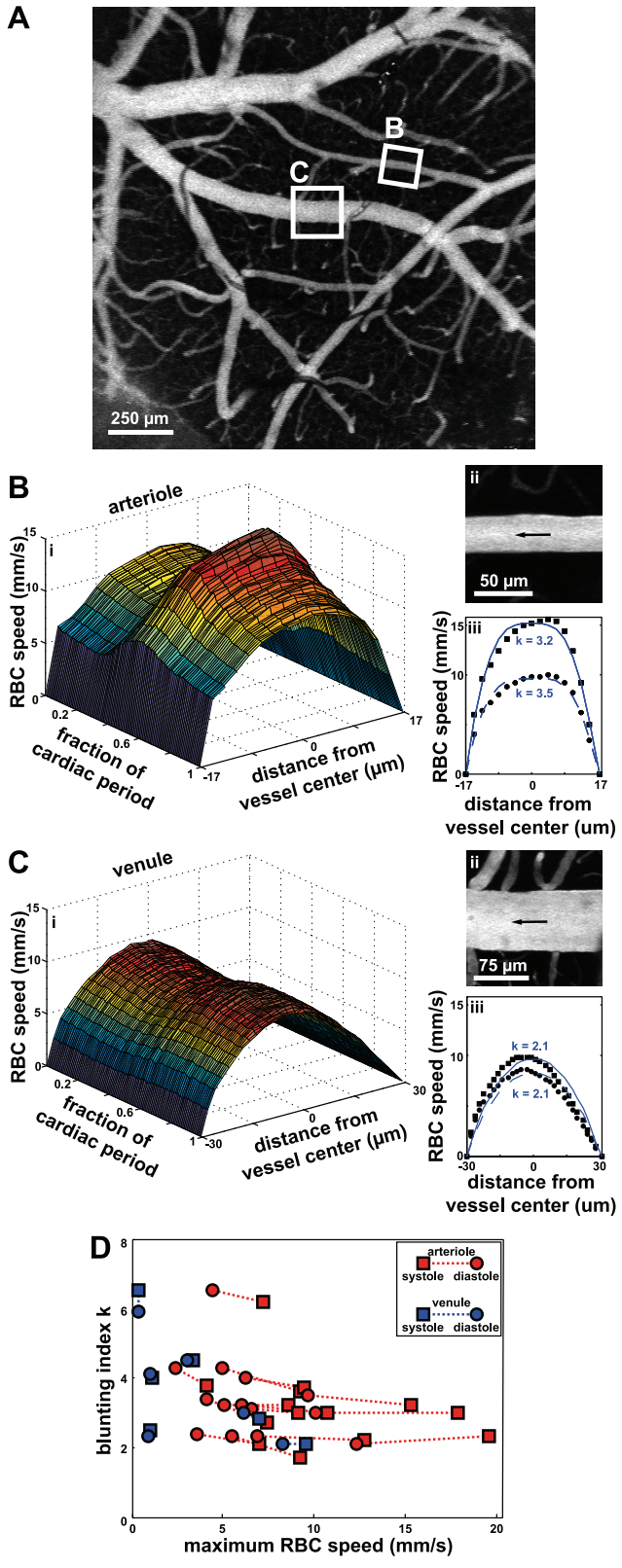

Pulsatile flow due to heartbeat. Pulsatile RBC flow was observed in all classes of cortical microvessels, including capillaries and venules, with a decreasing modulation depth from arterioles to capillaries to venules (Fig. 2*B*). In the majority of vessels of all classes, flow speed was modulated by heartbeat, although some of the slower capillaries and venules did not clearly show modulation. However, the variability in RBC speed was proportionally larger in these slower vessels, reducing our ability to resolve heartbeat-induced speed changes. As a result, the decrease in the number of vessels showing modulation with decreasing average flow speed may be due, in part, to this decreased sensitivity. Our data thus establish the minimum fraction of vessels whose flow speed is modulated by heartbeat. In previous work, heartbeat-induced speed modulation has been quantified in the aorta (43) and in large arteries (23) and veins (50) in the thoracic cavity of larger animals, such as pigs and dogs. Pulsatile flow has also been observed in surface arterioles and venules in the brain of rodents (38) and in 2-D microvascular beds such as the omentum and mesentery (39). Due to limitations in the spatial and temporal resolution as well as the flow speed measurement precision of previous approaches, the pulsatility of blood flow in cortical venules and microvessels $<$10-μm diameter was not observed until now. The magnitude of the heartbeat-induced speed modulation decreased in more distal vessels, consistent with dampening of the pressure pulse from the heartbeat as it travels through the distensible vascular network and loses energy to viscous damping (35) (Fig. 2*B*).

As expected, the interval between ventricular ejection and the time of maximum flow speed increased for more distal vessels (Fig. 2, *C* and *F*) because the pressure wave from the heartbeat must travel through the distensible vascular system (41). The interval between the time of maximal flow speed in penetrating arterioles and ascending venules was ~0.02 s, on average (Fig. 2*C*). In the mouse cortex, the shortest capillary path from a penetrating arteriole to an ascending venule has a median value of 490 μm [330- to 670-μm interquartile range, personal observations by P. Tsai based on data from Ref. (49)]. Using these data, we estimated the pulse wave velocity through the cortical capillary network to be ~25 mm/s.

In microvessels, the propagation of the pressure pulse from the heart is dominated by viscous forces and can be described by the following diffusion equation (11, 42):

$$\frac{d^2P}{dx^2} = GC\frac{dP}{dt} \qquad (4)$$

where P is the intraluminal pressure as a function of position along the vessel (x) and time (t), G is viscous resistance, and C is vascular compliance. The viscous resistance term is given by the following:

Fig. 5. RBC flow speed across the spatial profile of an arteriole and venule over the cardiac cycle. *A*: low-magnification 2PEF image of the fluorescently labeled brain vasculature. Boxes show regions measured in *B* and *C*. *B* and *C*: RBC speed from wall to wall across a surface arteriole (*B*,*i*) and a surface venule (*C*,*i*) over the cardiac cycle with corresponding 2PEF images of the vessels (*B*,*ii* and *C*,*ii*). The spatial flow speed profiles during systole and diastole are also shown (*B*,*iii* and *C*,*iii*). *D*: blunting index of surface arterioles and venules as a function of maximum RBC flow speed during systole and diastole, determined from fits of the flow profile at systole and diastole to *Eq. 3*.

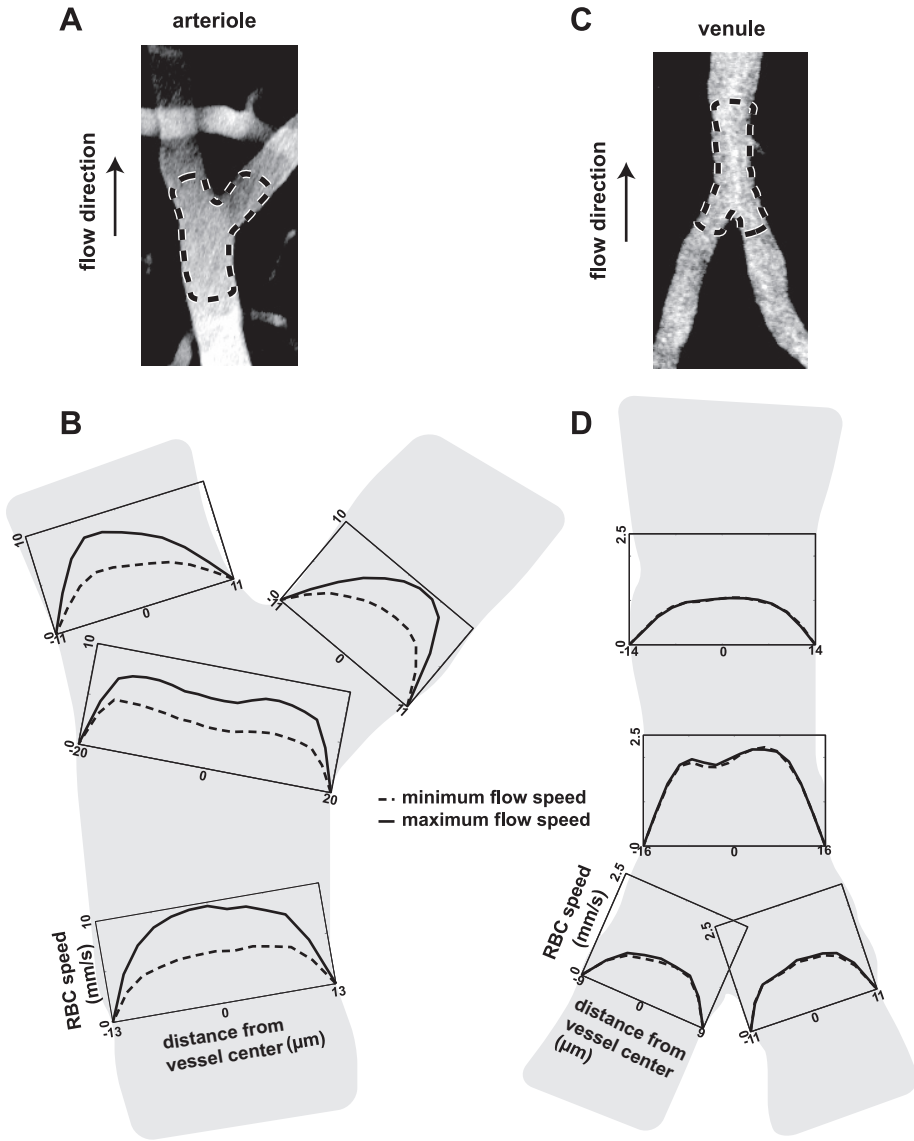

Fig. 6. Spatial RBC flow profiles upstream, at, and downstream of vascular junctions. *A*: 2PEF image of an arteriole bifurcation. *B*: wall-to-wall flow profiles in the upstream arteriole, at the bifurcation, and in the downstream branches during systole and diastole. *C* and *D*: 2PEF image of a venule merger (*C*) and corresponding flow profiles (*D*).

$$G = \frac{8\mu}{\pi R^4} \tag{5}$$

where μ is the viscosity of blood and R is the vessel radius. The vascular compliance is given by the following:

$$C = \frac{3\pi R^2(a+1)^2}{E(2a+1)} \tag{6}$$

where a is the ratio of vessel radius to vessel wall thickness and E is Young's modulus of the vessel wall. The solution to *Eq. 4* is a strongly damped oscillatory wave that propagates with a speed c given by the following:

$$c = \sqrt{\frac{2\omega}{GC}} \tag{7}$$

where ω is the angular frequency of the heartbeat. To determine the blood viscosity, we followed the approach of Ref. 37 using a tube hematocrit of 0.22 and a vessel radius of 2.9 μm (the averages for the capillaries in this study). We found the relative viscosity to be 1.2, which yielded a whole blood viscosity in the capillary bed of 1.6×10^{-3} Pa·s (52). Using the 25-mm/s pulse wave velocity we estimated experimentally, a vessel wall thickness of 0.5 μm (13), and the measured average 7.1-Hz heart rate, *Eq. 7* can be solved for Young's modulus of the vessel, giving a value of 0.12 MPa. This value for the modulus of brain capillaries is in fair agreement with measurements of microvessel modulus from rat spinotrapezius muscle (44) but smaller than previous estimates in the cat omentum and mesentery (18, 45).

Spatial flow profiles in surface arterioles and venules. Blood is composed of both cellular components and the liquid blood plasma. For arteries and veins, where the vessel diameter is much larger than the size of an RBC (6–8 μm) (15), whole blood can be approximated as a bulk fluid. For the microvessels considered in this study, the size of an RBC is a significant fraction of the vessel diameter. This leads to deviations from the parabolic flow profile expected for laminar flow of a Newtonian fluid (35), which is governed by Hagen-Poiseuille's law. In particular, blunting of the flow profile (i.e., exponent >

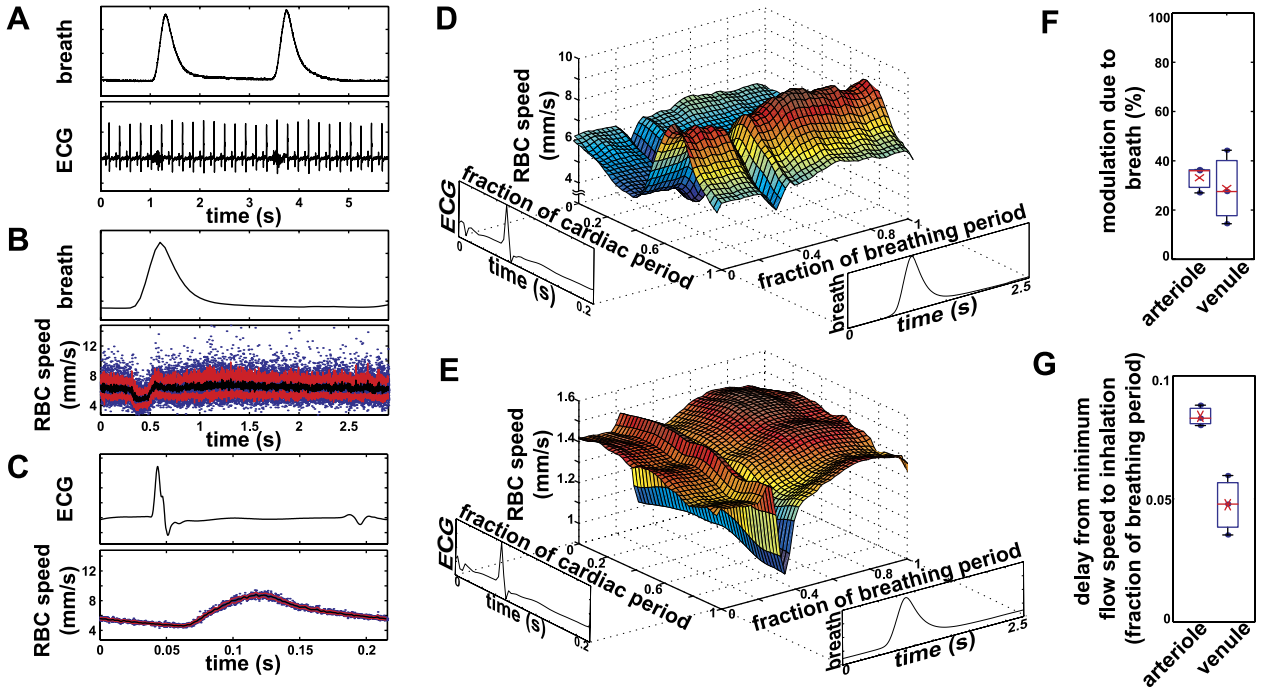

Fig. 7. Centerline RBC flow speed dependence on respiration and heartbeat. *A*: simultaneously recorded respiratory waveform and ECG. *B* and *C*: centerline RBC flow speed in an arteriole aligned relative to respiratory (*B*) and cardiac (*C*) cycles. *D* and *E*: two-dimensional plot of RBC flow speed in an arteriole (*D*) and a venule (*E*) as a function of both respiratory and cardiac cycle. *F* and *G*: boxplot of flow speed modulation due to breathing (*F*) and delay from the time of the respiration-dependent decrease in flow speed to inspiration (*G*) in surface arterioles and venules.

2) is expected in smaller vessels or in low-flow vessels, where RBCs tend to aggregate (35). The degree of blunting we observed in both arterioles (blunting index: 3.3 ± 1.1) and venules (blunting index: 3.7 ± 1.5; Fig. 5*D*) compare well with previous measurements of 2.4–4 for rabbit mesenteric arterioles (47). For surface arterioles, the blunting of the spatial profile was more pronounced during the diastolic phase in both our study (Fig. 5*D*) and in previous work (35), likely due to increased RBC aggregation at a lower shear rate (47).

Diverging and converging flow profiles. A previous study (26) has investigated blood flow at bifurcations of large arteries, which have fast flow speed and a high Reynold's number. In microcirculatory systems, detailed in vivo measurements of time- and space-dependent blood flow profiles at vessel junctions have not been made for vessels of <2 mm in diameter. In this study, we resolved the spatial flow profile at bifurcations and mergers of cortical surface arterioles and venules, respectively, and observed a double-peaked profile at the junction

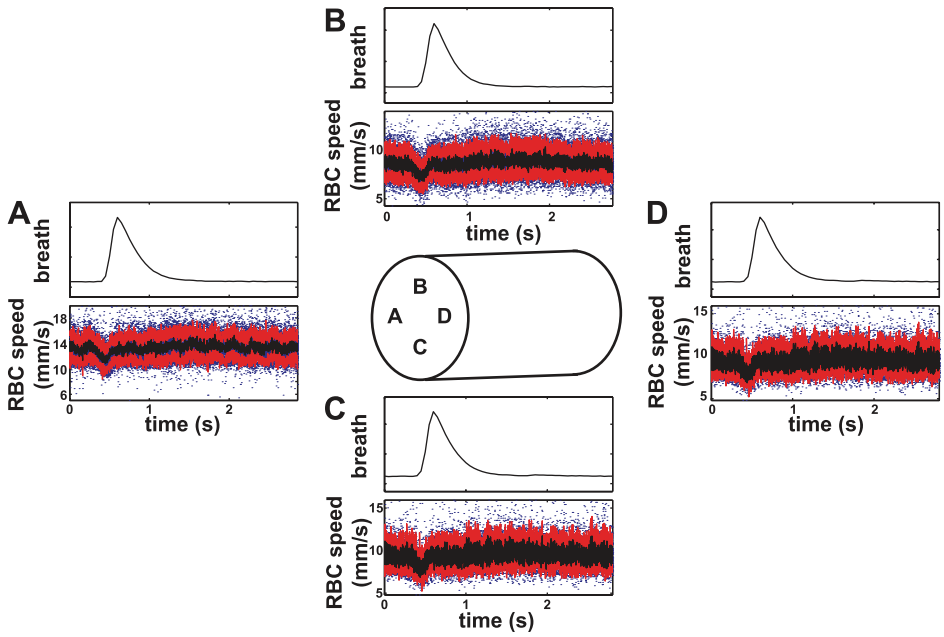

Fig. 8. Respiration-dependent flow speed fluctuations at different positions (*A*–*D*) inside the lumen of a 43-μm-diameter cortical arteriole. Each flow speed measurement was displaced ~10 μm from the vessel center in the direction indicated by the center schematic.

(Fig. 6, *B* and *D*). Interestingly, the flow profile of the two branches immediately downstream from an arteriole bifurcation displayed flow speed maxima that were skewed toward the outer edge of the bifurcation. This asymmetric flow profile is consistent with low Reynold's flow that is dominated by viscous forces and is skewed in the opposite direction than is found in bifurcations of larger vessels with faster flow speeds, such as the carotid bifurcation (26). After about one vessel diameter away from the junction, the spatial flow profiles shifted so the maximum speed was once again at the vessel center.

Blood flow speed modulation due to respiration. Breath inhalation was found to cause a transient decrease in centerline RBC flow speed in both cortical arterioles and venules (Fig. 7). The effect of breathing on blood flow speed has previously been examined in the vena cava, pulmonary artery and vein, and aorta in dogs (12, 25) and humans (50). During inspiration, the diaphragm movement creates a negative pressure in the thoracic cavity, allowing lung expansion and thus an increase in the total vascular volume of the lung. This causes a decrease in pulmonary return to the heart, which leads to a decrease in systemic blood pressure (25), although other studies have disagreed (12, 50). The transient flow speed decrease we observed in both surface arterioles and venules is consistent with such a decrease in systemic blood pressure during inhalation.

Comparison with other cerebral blood flow measurement modalities. Most current approaches for measuring cerebral hemodynamics focus on the quantification of regional changes in blood flow and do not resolve flow dynamics in individual microvessels. Clinical tools include MRI approaches, such as blood O_2 level-dependent MRI (4) and arterial spin labeling (5), as well as positron emission tomography (4, 17). These techniques are well suited to the measurement of regional changes of blood flow in the brain of humans and animal models with a spatial resolution of ~1 mm to 1 cm (4, 5, 17). Laser-Doppler spectroscopy (17), intrinsic optical imaging (48), and laser speckle contrast imaging (3) enable millimeter or better resolution mapping of flow changes in animal models, but still cannot resolve dynamics in individual microvessels. Doppler optical coherence tomography has recently emerged as an approach to mapping cerebral blood flow in many diving and ascending vessels simultaneously, but still cannot resolve flow in individual capillaries (46). Transcranial Doppler ultrasonography enables the measurement of detailed blood flow information, including pulsatile flow due to each heartbeat (17), but is unable to resolve blood flow in vessels smaller than the middle cerebral artery. It is optical microscopies that provide the necessary spatial and temporal resolution to quantify flow dynamics in vessels as small as capillaries. However, standard techniques, such as confocal microscopy, are limited in depth penetration by optical scattering (32). In vivo 2PEF microscopy overcomes some of these limitations and has allowed in vivo imaging of vascular topology and blood flow in murine brain to a depth of 1 mm (21). This technique relies on the nonlinear excitation of fluorescent molecules by tightly focused, infrared wavelength, femtosecond-duration laser pulses to restrict fluorescence emission to the focal volume, which is scanned in 3-D to form an image. With this tool, it is possible to image fluorescently labeled objects with micrometer resolution deep in the brain tissue of live, anesthetized rodents without damaging the tissue (9, 53). When the blood plasma is labeled with an intravenously injected fluorescent dye, this imaging method enables the in vivo mapping of the vascular architecture and, by directly tracking the motion of unlabeled RBCs, the quantification of flow speed in individual vascular segments (20, 40). This flow measurement technique, however, is able to quantify only the motion of RBCs, not of blood plasma. As a result, we are unable to characterize differences in average speed, or in temporal or spatial flow profiles, for blood plasma versus RBCs.

Conclusions. We have shown that 2PEF microscopy, together with ECG and respiratory waveform recordings, enables cerebral blood flow dynamics to be quantified with high spatial and temporal resolution and high flow speed precision in individual cerebral microvessels. The detailed information on cerebral hemodynamics obtained in this study and the experimental approach we developed has many applications. Because the disruption of blood flow in small cerebral vessels is associated with cognitive decline and dementia (33), our measurements of hemodynamics in cortical arterioles, capillaries, and venules can serve as a foundation for studies of altered brain blood flow in pathological conditions. Our discovery of pulsatile blood flow in brain capillaries is also of importance. Loss of pulsatile flow leads to increases in systematic vascular resistance and may cause tissue damage (51), while in pulmonary capillaries, pulsatile blood flow is essential for efficient O_2 transfer (51). Pulsatility may similarly be important for brain capillary function and neural tissue health. The interval between heartbeat and the time of maximum flow speed is an indicator of vascular health. Clinically, increases in pulse wave velocity are used to diagnose arterial stiffening (e.g., due to atherosclerosis), which is a contributing factor to cognitive decline and dementia (24). In addition, changes in the microcirculation that contribute to the central nervous system damage that results from chronic hypertension may depend, in part, on the abnormal transmission of highly pulsatile blood pressure into the microvascular networks of the brain (and other highly perfused organs with low vascular resistance) (33). Our experimental approach allows these important hemodynamic phenomena to be investigated in the murine brain vasculature. When combined with transgenic animals, this approach may allow in-depth studies of the role of microvascular dysfunction in a variety of brain diseases, including Alzheimer's disease and vascular dementia. Previous work (14) has found that endothelial cells experiencing low shear or turbulent flow become seed sites for the formation of atherosclerotic plaques and that such flow disturbances are common at arterial bifurcations. Our method to quantify flow profiles in individual microvessels and at microvascular junctions could enable the investigation of potentially pathogenic flow in these small-diameter vessels. The ability to carefully quantify these blood flow dynamics, as well investigate how hemodynamics may change in pathological conditions, provides a new window on the normal and disease-state cerebral microcirculation.

ACKNOWLEDGMENTS

The authors thank Nelson Zhou for assistance with the design and construction of the breathing monitor and IMRA America, Incorporated, for the loan of laser equipment.

GRANTS

This work was funded by a Med-Into-Grad fellowship from the Howard Hughes Medical Institute (to T. P. Santisakultarm), National Institute on Aging Postdoctoral Fellowship 1-F32-AG-031620 (to N. Nishimura), a L'Oréal USA Fellowship for Women in Science fellowship (to N. Nishimura), and a grant from the Cancer Research and Treatment Fund, Incorporated (to C. B. Schaffer).

DISCLOSURES

No conflicts of interest, financial or otherwise, are declared by the author(s).

AUTHOR CONTRIBUTIONS

Author contributions: T.P.S., N.N., W.L.O., and C.B.S. conception and design of research; T.P.S. and N.N. performed experiments; T.P.S., N.R.C., and P.C.D. analyzed data; T.P.S., N.N., A.I.S., R.T.S., W.L.O., and C.B.S. interpreted results of experiments; T.P.S. prepared figures; T.P.S. drafted manuscript; T.P.S., N.N., A.I.S., R.T.S., and C.B.S. edited and revised manuscript; T.P.S., N.R.C., N.N., A.I.S., R.T.S., P.C.D., W.L.O., and C.B.S. approved final version of manuscript.

REFERENCES

1. **Audet D, Olbricht W.** The motion of model cells at capillary bifurcations. *Microvasc Res* 33: 377–396, 1987.
2. **Blinder P, Shih AY, Rafie C, Kleinfeld D.** Topological basis for the robust distribution of blood to rodent neocortex. *Proc Natl Acad Sci USA* 107: 12670–12675, 2010.
3. **Boas DA, Dunn AK.** Laser speckle contrast imaging in biomedical optics. *J Biomed Opt* 15: 011109, 2010.
4. **Bulte DP, Kelly M, Germuska M, Xie J, Chappell MA, Okell TW, Bright MG, Jezzard P.** Quantitative measurement of cerebral physiology using respiratory-calibrated MRI. *Neuroimage* 60: 582–591, 2011.
5. **Buxton RB, Frank LR.** A model for the coupling between cerebral blood flow and oxygen metabolism during neural stimulation. *J Cereb Blood Flow Metab* 17: 64–72, 1997.
6. **Constantinescu AA, Vink H, Spaan JA.** Elevated capillary tube hematocrit reflects degradation of endothelial cell glycocalyx by oxidized LDL. *Am J Physiol Heart Circ Physiol* 280: H1051–H1057, 2001.
7. **Cruickshank K, Riste L, Anderson SG, Wright JS, Dunn G, Gosling RG.** Aortic pulse-wave velocity and its relationship to mortality in diabetes and glucose intolerance: an integrated index of vascular function? *Circulation* 106: 2085–2090, 2002.
8. **Cuzick J.** A Wilcoxon-type test for trend. *Stat Med* 4: 87–90, 1985.
9. **Denk W, Strickler J, Webb W.** Two-photon laser scanning fluorescence microscopy. *Science* 248: 73–76, 1990.
10. **Drew P, Blinder P, Cauwenberghs G, Shih A, Kleinfeld D.** Rapid determination of particle velocity from space-time images using the Radon transform. *J Comput Neurosci* 29: 5–11, 2010.
11. **Gross JF, Intaglietta M, Zweifach BW.** Network model of pulsatile hemodynamics in the microcirculation of the rabbit omentum. *Am J Physiol* 226: 1117–1123, 1974.
12. **Guntheroth WG, Morgan BC, Mullins GL.** Effect of respiration on venous return and stroke volume in cardiac tamponade. Mechanism of pulsus parodoxus. *Circ Res* 20: 381–390, 1967.
13. **Guyton AC, Hall JE.** *Textbook of Medical Physiology*. New York: Saunders, 2005.
14. **Hahn C, Schwartz MA.** The role of cellular adaptation to mechanical forces in atherosclerosis. *Arterioscler Thromb Vasc Biol* 28: 2101–2107, 2008.
15. **Hawkey CM, Bennett PM, Gascoyne SC, Hart MG, Kirkwood JK.** Erythrocyte size, number and haemoglobin content in vertebrates. *Br J Haematol* 77: 392–397, 1991.
16. **Heinicke K, Baum O, Ogunshola OO, Vogel J, Stallmach T, Wolfer DP, Keller S, Weber K, Wagner PD, Gassmann M, Djonov V.** Excessive erythrocytosis in adult mice overexpressing erythropoietin leads to hepatic, renal, neuronal, and muscular degeneration. *Am J Physiol Regul Integr Comp Physiol* 291: R947–R956, 2006.
17. **Heiss W, Forsting M, Diener H.** Imaging in cerebrovascular disease. *Curr Opin Neurol* 14: 67–75, 2001.
18. **Intaglietta M, Richardson DR, Tompkins WR.** Blood pressure, flow, and elastic properties in microvessels of cat omentum. *Am J Physiol* 221: 922–928, 1971.
19. **Kleinfeld D, Delaney KR.** Distributed representation of vibrissa movement in the upper layers of somatosensory cortex revealed with voltage-sensitive dyes. *J Comp Neurol* 375: 89–108, 1996.
20. **Kleinfeld D, Mitra P, Helmchen F, Denk W.** Fluctuations and stimulus-induced changes in blood flow observed in individual capillaries in layers 2 through 4 of rat neocortex. *Proc Natl Acad Sci USA* 95: 15741–15746, 1998.
21. **Kobat D, Durst ME, Nishimura N, Wong AW, Schaffer CB, Xu C.** Deep tissue multiphoton microscopy using longer wavelength excitation. *Opt Express* 17: 13354–13364, 2009.
22. **Lorthois S, Cassot F, Lauwers F.** Simulation study of brain blood flow regulation by intra-cortical arterioles in an anatomically accurate large human vascular network: part I: methodology and baseline flow. *Neuroimage* 54: 1031–1042, 2011.
23. **Mills C, Gabe I, Gault J, Mason D, Ross J, Braunwald E, Shillingford J.** Pressure-flow relationships and vascular impedance in man. *Cardiovasc Res* 4: 405–417, 1970.
24. **Mitchell GF, Van Buchem MA, Sigurdsson S, Gotal JD, Jonsdottir MK, Kjartansson O, Garcia M, Aspelund T, Harris TB, Gudnason V, Launer LJ.** Arterial stiffness, pressure and flow pulsatility and brain structure and function: the age, gene/environment susceptibility–Reykjavik study. *Brain* 134: 3398–3407, 2011.
25. **Morgan B, Dillard D, Guntheroth W.** Effect of cardiac and respiratory cycle on pulmonary vein flow, pressure, and diameter. *J Appl Physiol* 21: 1276–1280, 1966.
26. **Motomiya M, Karino T.** Flow patterns in the human carotid artery bifurcation. *Stroke* 15: 50–56, 1984.
27. **Neu B, Wenby R, Meiselman HJ.** Effects of dextran molecular weight on red blood cell aggregation. *Biophys J* 95: 3059–3065, 2008.
28. **Nguyen J, Nishimura N, Fetcho RN, Iadecola C, Schaffer CB.** Occlusion of cortical ascending venules causes blood flow decreases, reversals in flow direction, and vessel dilation in upstream capillaries. *J Cereb Blood Flow Metab* 31: 2243–2254, 2011.
29. **Nguyen Q, Tsai P, Kleinfeld D.** MPScope: a versatile software suite for multiphoton microscopy. *J Neurosci Methods* 156: 351–359, 2006.
30. **Nishimura N, Rosidi NL, Iadecola C, Schaffer CB.** Limitations of collateral flow after occlusion of a single cortical penetrating arteriole. *J Cereb Blood Flow Metab* 30: 1914–1927, 2010.
31. **Nishimura N, Schaffer C, Friedman B, Tsai P, Lyden P, Kleinfeld D.** Targeted insult to subsurface cortical blood vessels using ultrashort laser pulses: three models of stroke. *Nat Methods* 3: 99–108, 2006.
32. **Nyman L, Wells K, Head W, McCaughey M, Ford E, Brissova M, Piston D, Powers A.** Real-time, multidimensional in vivo imaging used to investigate blood flow in mouse pancreatic islets. *J Clin Invest* 118: 3790–3797, 2008.
33. **O'Brien J.** Vascular cognitive impairment. *Am J Geriatr Psychiatry* 14: 724–733, 2006.
34. **Pantoni L.** Cerebral small vessel disease: from pathogenesis and clinical characteristics to therapeutic challenges. *Lancet Neurol* 9: 689–701, 2010.
35. **Popel AS, Johnson PC.** Microcirculation and hemorheology. *Annu Rev Fluid Mech* 37: 43–69, 2005.
36. **Pries A, Ley K, Claassen M, Gaehtgens P.** Red cell distribution at microvascular bifurcations. *Microvasc Res* 38: 81–101, 1989.
37. **Pries AR, Neuhaus D, Gaehtgens P.** Blood viscosity in tube flow: dependence on diameter and hematocrit. *Am J Physiol Heart Circ Physiol* 263: H1770–H1778, 1992.
38. **Rosenblum W.** Erythrocyte velocity and a velocity pulse in minute blood vessels on the surface of the mouse brain. *Circ Res* 24: 887–892, 1969.
39. **Salotto AG, Muscarella LF, Melbin J, Li JK, Noordergraaf A.** Pressure pulse transmission into vascular beds. *Microvasc Res* 32: 152–163, 1986.
40. **Schaffer C, Friedman B, Nishimura N, Schroeder L, Tsai P, Ebner F, Lyden P, Kleinfeld D.** Two-photon imaging of cortical surface microvessels reveals a robust redistribution in blood flow after vascular occlusion. *PLoS Biol* 4: e22, 2006.
41. **Schmid-Schonbein G.** Biomechanics of microcirculatory blood perfusion. *Annu Rev Biomed Eng* 1: 73–102, 1999.

42. **Schmid-Schönbein GW, Lee SY, Sutton D.** Dynamic viscous flow in distensible vessels of skeletal muscle microcirculation: application to pressure and flow transients. *Biorheology* 26: 215–227, 1989.
43. **Seed W, Wood N.** Velocity patterns in the aorta. *Cardiovasc Res* 5: 319–330, 1971.
44. **Skalak TC, Schmid-Schonbein GW.** Viscoelastic properties of microvessels in rat spinotrapezius muscle. *J Biomech Eng* 108: 193–200, 1986.
45. **Smaje LH, Fraser PA, Clough G.** The distensibility of single capillaries and venules in the cat mesentery. *Microvasc Res* 20: 358–370, 1980.
46. **Srinivasan VJ, Atochin DN, Radhakrishnan H, Jiang JY, Ruvinskaya S, Wu W, Barry S, Cable AE, Ayata C, Huang PL, Boas DA.** Optical coherence tomography for the quantitative study of cerebrovascular physiology. *J Cereb Blood Flow Metab* 31: 1339–1345, 2011.
47. **Tangelder G, Slaaf D, Muijtjens A, Arts T, oude Egbrink M, Reneman R.** Velocity profiles of blood platelets and red blood cells flowing in arterioles of the rabbit mesentery. *Circ Res* 59: 505–514, 1986.
48. **Ts'o DY, Frostig RD, Lieke EE, Grinvald A.** Functional organization of primate visual cortex revealed by high resolution optical imaging. *Science* 249: 417–420, 1990.
49. **Tsai P, Kaufhold J, Blinder P, Friedman B, Drew P, Karten H, Lyden P, Kleinfeld D.** Correlations of neuronal and microvascular densities in murine cortex revealed by direct counting and colocalization of nuclei and vessels. *J Neurosci* 29: 14553–14570, 2009.
50. **Wexler L, Bergel D, Gabe I, Makin G, Mills C.** Velocity of blood flow in normal human venae cavae. *Circ Res* 23: 349–359, 1968.
51. **Wilkens H, Regelson W, Hoffmeister FS.** The physiolgic importance of pulsatile blood flow. *N Engl J Med* 267: 443–446, 1962.
52. **Windberger U, Bartholovitsch A, Plasenzotti R, Korak KJ, Heinze G.** Whole blood viscosity, plasma viscosity and erythrocyte aggregation in nine mammalian species: reference values and comparison of data. *Exp Physiol* 88: 431–440, 2003.
53. **Zipfel W, Williams R, Webb W.** Nonlinear magic: multiphoton microscopy in the biosciences. *Nat Biotechnol* 21: 1369–1377, 2003.
54. **Zweifach BW, Lipowsky HH.** Quantitative studies of microcirculatory structure and function. III. Microvascular hemodynamics of cat mesentery and rabbit omentum. *Circ Res* 41: 380–390, 1977.